

# Interfacial stabilization for inverted perovskite solar cells with long-term stability

Zhubing He (✉ [hezb@sustech.edu.cn](mailto:hezb@sustech.edu.cn))

Southern University of Science and Technology <https://orcid.org/0000-0002-2775-0894>

Wei Chen

The University of Hong Kong

Bing Han

Southern University of Science and Technology (SUSTech)

Qin Hu

Materials Sciences Division, Lawrence Berkeley National Laboratory

Meng Gu

Southern University of Science and Technology <https://orcid.org/0000-0002-5126-9611>

Yudong Zhu

Southern University of Science and Technology (SUSTech)

Wenqiang Yang

Peking University

Yecheng Zhou

Southern University of Science and Technology (SUSTech)

Deying Luo

Peking University

Fangzhou Liu

The university of Hong Kong

Rui Cheng

The university of Hong Kong

Rui Zhu

Peking University <https://orcid.org/0000-0001-7631-3589>

Shien-Ping Feng

The University of Hong Kong <https://orcid.org/0000-0002-3941-1363>

Aleksandra Djurišić

The university of Hong Kong

Thomas Russell

University of Massachusetts Amherst <https://orcid.org/0000-0001-6384-5826>

**Keywords:** Perovskite solar cells, interfacial stabilization, metal electrode corrosion

**Posted Date:** August 28th, 2020

**DOI:** <https://doi.org/10.21203/rs.3.rs-64280/v1>

**License:**   This work is licensed under a Creative Commons Attribution 4.0 International License.

[Read Full License](#)

---

## **Interfacial stabilization for inverted perovskite solar cells with long-term stability**

Wei Chen<sup>1,2,†</sup> Bing Han<sup>1†</sup> Qin Hu,<sup>3,7†</sup> Meng Gu,<sup>1</sup> Yudong Zhu,<sup>1</sup> Wenqiang Yang,<sup>4</sup> Yecheng Zhou,<sup>5</sup> Deying Luo,<sup>4</sup> Fang-Zhou Liu,<sup>2</sup> Rui Cheng,<sup>6</sup> Rui Zhu,<sup>4</sup> Shien Ping Feng,<sup>6</sup> Aleksandra B. Djurišić,<sup>2\*</sup> Thomas P. Russell<sup>3,7\*</sup> and Zhubing He<sup>1\*</sup>

<sup>1</sup>Department of Materials Science and Engineering, Shenzhen Key Laboratory of Full Spectral Solar Electricity Generation (FSSEG), Southern University of Science and Technology, No. 1088, Xueyuan Rd., Shenzhen, 518055, Guangdong, P.R. China.

<sup>2</sup>Department of Physics, The University of Hong Kong, Pokfulam, Hong Kong SAR.

<sup>3</sup>Materials Sciences Division, Lawrence Berkeley National Laboratory, Berkeley, California 94720, USA.

<sup>4</sup>State Key Laboratory for Artificial Microstructure and Mesoscopic Physics, Department of Physics, Peking University, Beijing 100871, China.

<sup>5</sup>Department of Physics, Southern University of Science and Technology, No. 1088, Xueyuan Rd., Shenzhen, 518055, Guangdong, P.R. China.

<sup>6</sup>Department of Mechanical Engineering, The University of Hong Kong, Pokfulam, Hong Kong SAR.

<sup>7</sup>Department of Polymer Science and Engineering, University of Massachusetts, Amherst, Massachusetts 01003, United States.

<sup>†</sup>These authors contributed to this work equally.

**Abstract:**

Perovskite solar cells (PSCs) commonly exhibit significant performance degradation due to ion migration through the top charge transport layer and ultimately metal electrode corrosion. Here, we demonstrate an interfacial management strategy using a boron chloride subphthalocyanine ( $\text{Cl}_6\text{SubPc}$ )/fullerene electron-transport layer, which not only passivates the interfacial defects in the perovskite, but also suppresses halide diffusion as evidenced by multiple techniques, including visual element mapping by electron energy loss spectroscopy. As a result, we obtain inverted PSCs with an efficiency of 22.0% (21.3% certified), shelf life of 7000 hours,  $T_{80}$  of 816 h under damp heat stress (compared to less than 20 h without  $\text{Cl}_6\text{SubPc}$ ), and initial performance retention of 98% after 2000 hours at 80 °C in inert environment, 90% after 2034 h of illumination and MPP tracking in ambient for encapsulated devices and 95% after 1272 h outdoor testing ISOS-O-1, which is among the top device performance for the inverted PSCs.

## Introduction

Metal halide perovskite solar cells (PSCs) have exhibited significant progress in terms of both conversion efficiency and stability in recent years.<sup>1-6</sup> However, the device stability is not sufficient for the commercialization, and, hence, is more crucial than conversion efficiency at present.<sup>7</sup> Whether conventional *n-i-p* or inverted *p-i-n* devices are used, PSCs commonly exhibit degradation when exposed to moisture, ambient atmosphere, heat, and electric bias.<sup>4,7,8</sup> The degradation initiates from defect sites near the surfaces upon exposure to light, moisture, oxygen, and heat, and these defects also initiate ion migration, resulting in reactions of the perovskite (PVK) at the charge transporting interfaces and the electrodes.<sup>8</sup>

Of the different device architectures, inverted PSCs are of particular interest, since the absence of doped organic charge transport layer on top of the perovskite enables superior thermal stability in comparison to conventional devices,<sup>9</sup> and high stability under combined light and heat stressing<sup>10</sup> and thermal cycling.<sup>11</sup> In addition, they also exhibit improved stability under reverse bias compared to conventional devices.<sup>3,9,12</sup> It is well known that the PVK/charge transport layer, namely hole transport layer (HTL) or electron transport layer (ETL) dominate conversion efficiency and stability of devices mainly by affecting interfacial defect density and ions diffusion.<sup>3,13</sup> In an inverted device structure, the top PVK/ETL interface is expected to significantly influence the device stability due to its effect on moisture and oxygen penetration into the perovskite and halide ion diffusion to the electrode. It is well recognized that inverted PSCs with commonly used fullerene-based ETLs not only exhibit significant

interfacial recombination losses,<sup>6,13,14</sup> but also have susceptibility to the oxygen and moisture ingress into the devices.<sup>4,15</sup> In addition, their thermal stability is limited by the aggregation of fullerene acceptor, which leads to the deterioration of contact between PVK and ETL.<sup>4</sup> More importantly, volatile perovskite decomposition products readily diffuse through the fullerene-based layer,<sup>15</sup> exacerbating PVK and electrode degradation, since almost all metals react with PVK decomposition products,<sup>4</sup> and leading to shunting at low reverse bias voltages.<sup>16</sup>

Therefore, interfacial stabilization at the interface of PVK/ETL is crucial for achieving both high efficiencies and long-term stabilities in inverted *p-i-n* PSCs. While the performance improvements have been demonstrated by various approaches,<sup>3,6,13,15,17-22</sup> including the use of different inorganic<sup>13,17</sup> or organic<sup>15,18-20</sup> interfacial layers between PVK and C<sub>60</sub>, further performance improvements are still needed to bring these devices closer to commercialization.<sup>7</sup> Here we use a boron chloride subphthalocyanine (Cl<sub>6</sub>SubPc)/fullerene ETL to simultaneously reduce the interfacial defect density and hinder ion migration, resulting in power conversion efficiencies of 22.0% (certified 21.3 %), a shelf life of 7000 hours, T<sub>80</sub> of 816 h under damp heat stress, and performance retention of 98% after 2000 hours at 80 °C in inert environment, and 95% after 1200 h outdoor testing (first outdoor performance test for inverted devices). Dramatic inhibition of the iodide diffusion, as evidenced by multiple experimental techniques can be attributed to the unique properties of Cl<sub>6</sub>SubPc, forms strong Pb-Cl bonds, contributing to defect passivation, and has strong interactions with iodine, that effectively suppresses ion migration and electrode corrosion even under

extreme conditions of reverse bias under illumination.

Phthalocyanine and porphyrin have excellent thermal and photochemical stability and have been used in different types of solar cells, including PSCs<sup>23</sup> and OPVs.<sup>24,25</sup> Phthalocyanine- and porphyrin-related molecules exhibit one intriguing aspect, namely their high iodine adsorption capacity and general capability of adsorption of various guest molecules owing to their cloud of  $\pi$  electrons.<sup>26</sup> This aspect of phthalocyanine-related molecules has been little explored in PSCs, but potentially offers a route to inhibit ion migration and/or diffusion of perovskite decomposition products through the ETL, protecting the electrode from corrosion. Thus, we investigated the use of a chlorinated macrocyclic molecule, Cl<sub>6</sub>SubPc, which has been previously used as an acceptor in OPVs.<sup>24,25</sup> The chemical structure of Cl<sub>6</sub>SubPc and the device architecture of *p-i-n* planar PSCs are shown in **Figures 1a and 1b**. We use inorganic Cu doped NiO<sub>x</sub> nanoparticles as the HTL and C<sub>60</sub> as the ETL,<sup>27</sup> and a Cs<sup>+</sup>, formamidinium (FA<sup>+</sup>) and methylammonium (MA<sup>+</sup>) (CsFAMA) cations mixed perovskite<sup>28,29</sup> as the active layer. We investigated both CsFAMA perovskites, labeled as 3D PVK, and CsFAMA perovskites with the surface treated with phenyl ethyl-ammonium iodide (PEAI) solution, labeled as 3D/2D PVK (for experimental details, see Methods, Supplementary Information). The use of a PEA solution treatment to form a 2D capping layer on top of the perovskite has been investigated, since a low dimensional perovskite capping layers passivates surface defects and improves the perovskite stability.<sup>30</sup> The Cl<sub>6</sub>SubPc and C<sub>60</sub> bilayer ETL was then thermally evaporated on top of the perovskites.

The performances of different devices are shown in **Figure 1 c-h** and

**Supplementary Figures 1-3**, and summarized in **Supplementary Tables 1** and **2**. The performance of 3D PVK devices for both ETLs is inferior to that of 3D/2D devices, in agreement with literature reports.<sup>30</sup> We also observe that CsFAMA 3D PVK devices with thin Cl<sub>6</sub>SubPc (20 nm) ETLs exhibited a relatively low efficiency of 19.3%, due to the low J<sub>sc</sub> and V<sub>oc</sub>. This may arise from the mismatch of the energy levels at the interface which hinders electron transfer, due to the relatively high LUMO level (~3.8 eV)<sup>24</sup> of Cl<sub>6</sub>SubPc. The up-shift of the conduction band of 3D/2D PVK in comparison to 3D PVK (from ~4.0 eV to ~3.8 eV)<sup>30</sup> could enable improved electron collection and for the 3D/2D PVK/ Cl<sub>6</sub>SubPc devices an increase of the PCE to 20.5%. Similar improvements are seen for the 3D/2D PVK/C60 devices, where the efficiency increases from 20.2% to 20.8% (**Supplementary Table 1**).



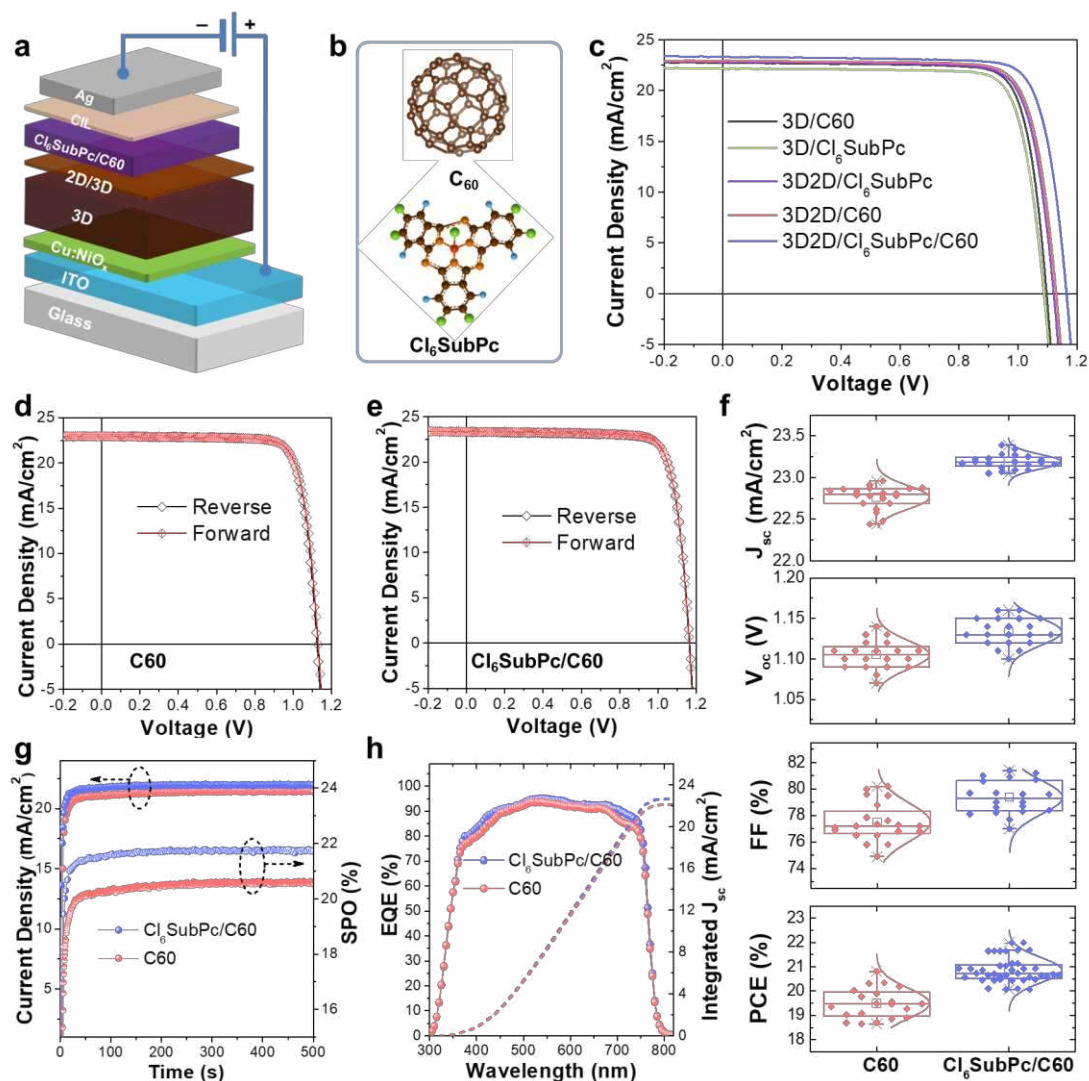


**Figure 1.** a) Device architecture of the inverted planar perovskite solar cells (PSCs); b) Molecular structures of the C<sub>60</sub> and chlorinated macrocyclic molecule (Cl<sub>6</sub>SubPc) ETLs; c) J-V curves of the PSCs with various ETLs (reverse scan) under 1 sun illumination; d-e) J-V curves of the optimal 3D/2D/C<sub>60</sub> (d) and 3D/2D/Cl<sub>6</sub>SubPc/C<sub>60</sub> (e) devices under reverse and forward scan directions; f) Device performance statistics for 3D/2D/C<sub>60</sub> and 3D/2D/Cl<sub>6</sub>SubPc/C<sub>60</sub> devices; g) Steady power output (SPO) of the optimal 3D/2D/C<sub>60</sub> and 3D/2D/Cl<sub>6</sub>SubPc/C<sub>60</sub> devices test at the bias of maximum power point; h) EQE spectra for the optimal 3D/2D/C<sub>60</sub> and 3D/2D/Cl<sub>6</sub>SubPc/C<sub>60</sub> devices.

Since non-fullerene ETLs offer a compromise between efficiency and stability when employed as interlayer between the perovskite and fullerene,<sup>20</sup> we also investigated the performance of devices with Cl<sub>6</sub>SubPc/C<sub>60</sub> bilayer ETL for different

Cl<sub>6</sub>SubPc thicknesses, as shown in **Supplementary Figure 2**. For optimal Cl<sub>6</sub>SubPc thickness of 8 nm, the PCE can be further improved to 22.0% (with a V<sub>oc</sub> of 1.16 V, a J<sub>sc</sub> of 23.31 mA/cm<sup>2</sup> and a high FF of 81.2 %) by using the 3D/2D PVK/ Cl<sub>6</sub>SubPc/C60 (8/20 nm) structure, as shown in **Figure 1c** and **Supplementary Table 1**. Both devices with C60 and Cl<sub>6</sub>SubPc/C60 ETLs show negligible I-V hysteresis (**Figure 1d and 1e**). Significant improvements in the performance when using Cl<sub>6</sub>SubPc are evident from the steady power output (**Figure 1g**) and external quantum efficiency (EQE) curves (**Figure 1f**), and the integrated J<sub>sc</sub> values from EQE spectra are consistent with the I-V results. The statistical distribution of device performances is shown in Figure 1f, and summarized in **Supplementary Table 2**. To verify the reliability of the device performance, a non-encapsulated device in air at 63% ambient humidity was certified at a PCE of 21.3% (The National Institute of Metrology (NIM), **Supplementary Figure 3**). This efficiency is among the best reported for *p-i-n* PSCs (**Supplementary Table 3**), and is the highest certified efficiency for planar inverted PSCs with inorganic HTLs. Furthermore, the devices with Cl<sub>6</sub>SubPc/C60 ETL exhibited similar high performance with different electrodes, as shown in (**Supplementary Figure 4 and Supplementary Table 4**), indicating the broad process window for our interfacial modification strategy.

To understand the observed performance improvements, we performed comprehensive morphological, compositional and structural characterizations of the devices. From the SEM images and XRD patterns (**Supplementary Figure 5**), we observe an increase in grain size and a decrease of diffraction peak intensity of PbX<sub>2</sub> (PbI<sub>2</sub>/PbBr<sub>2</sub>) (~12.7°) in 3D/2D PVK samples. The impact of 2D capping layers and

the additional Cl<sub>6</sub>SubPc ETL on the perovskite morphology and crystallinity were investigated using grazing-incidence wide-angle X-ray scattering (GIWAXS). As shown in **Supplementary Figure 6**, an isotropic scattering profile (azimuthally uniform diffraction rings) at high  $q$  values ( $q > 1 \text{ \AA}^{-1}$ ), indicate a random orientation of the crystal grains in 3D PVK films. After passivation with PEAI, we observe sharp Bragg diffraction spots in the out-of-plane (OOP) direction at low  $q$  values ( $q < 0.9 \text{ \AA}^{-1}$ ), indicating the formation of 2D PVK oriented parallel to the surface of the 3D PVK surface (**Supplementary Figure 6b and c**).<sup>31,32</sup> **Supplementary Figures 7a and b** show that Cl<sub>6</sub>SubPc is amorphous with no obvious diffraction features of Cl<sub>6</sub>SubPc for the 3D/2D PVK/Cl<sub>6</sub>SubPc sample. We note that the arc shape at  $q \sim 0.9 \text{ \AA}^{-1}$  suggests a PbX<sub>2</sub> (PbI<sub>2</sub> and/or PbBr<sub>2</sub>) residue. 1D azimuthal integrated scattering profiles are shown in **Supplementary Figure 8**. We can observe a decrease in PbX<sub>2</sub> content (peak ratios of signature peaks at  $q \sim 0.91 \text{ \AA}^{-1}$  and  $q \sim 1.0 \text{ \AA}^{-1}$  are assigned to the (001) plane of PbX<sub>2</sub> crystal and (110) plane of 3D PVK) in 2D/3D PVK compared to 3D PVK. The improvement in crystallinity after PEAI treatment is in agreement with the surface induced secondary grain growth observed upon treating halide perovskite surfaces with organic ammonium solution.<sup>33</sup> Surprisingly, the deposition of Cl<sub>6</sub>SubPc also induced further changes in the crystal structure. We observe reduced FWHMs (full width at half maximum) of the reflection at  $q \sim 0.28 \text{ \AA}^{-1}$  and  $q \sim 0.38 \text{ \AA}^{-1}$  (OOP) of the 2D perovskites Cl<sub>6</sub>SubPc, increased ratio of the areas of the reflection at  $q \sim 0.77 \text{ \AA}^{-1}$  for 2D PVSK to the reflection at  $q \sim 1.0 \text{ \AA}^{-1}$  for CsFAMA PVK, as well as reduced peaks of the hexagonal non-PVK phase ( $\delta$  phase) at  $q \sim 0.85 \text{ \AA}^{-1}$  (OOP) and PbX<sub>2</sub> at  $q \sim 0.91 \text{ \AA}^{-1}$ ,

indicating improved crystallinity. One possible mechanism behind the observed phenomenon is that Cl<sub>6</sub>SubPc caused surface-induced secondary grain growth after the deposition of organic molecules on the surface of the perovskite to minimize the interfacial energy, facilitated by the low activation energies for ion diffusion, low elastic modulus and consequent liquid-like behavior of the soft perovskite lattice.<sup>33</sup> Even though the reasons for the observed changes after Cl<sub>6</sub>SubPc deposition are not fully clear. However, it should be noted that recrystallization of the perovskite can not only be induced by organic ammonium molecule surface treatment, but also over time in the presence of strong chemical interactions with the electrode in HTL-free PSCs.<sup>34</sup> To gain further insight into the structure of the films and possible effects of Cl<sub>6</sub>SubPc, we performed cross-sectional cryogenic-transmission electron microscopy (cryo-TEM), as well as theoretical calculations of interactions between Cl<sub>6</sub>SubPc and the perovskite. Cryo-TEM images and the electron energy loss spectroscopy (EELS) mapping images are shown in **Figure 2 a-g**. As shown in **Figure 2b**, the higher magnification image of perovskites at the interface of ETL/PVK shows the surface layer of perovskite is composed of both 3D and 2D perovskites. The Fourier transformed electron diffraction (FTED) pattern from the high resolution transmission electron microscopy (HRTEM) image shows 3D CsFAMA PVK is a typical cubic phase with lattice parameters ( $a = b$ ) of 3.2 Å (**Figure 2c**), which is in agreement with the result of XRD patterns (**Supplementary Figure 5**) and similar to the previous reports of 3D PVK.<sup>35,36</sup> Enlarged lattice of the (110)<sub>C</sub> plane can clearly distinguish the identical position of [PbI<sub>6</sub>]<sup>4-</sup> octahedra and cations (**Figure 2e**), which is also shown schematically for clear

understanding. For 2D PVK shown in **Figure 2d**, the lattice and FTED are different from that 3D PVK. Observed lattice distance of 7.1 Å corresponding to n=1 is consistent with the 0.88 Å<sup>-1</sup> peak in both in plane and out of plane patterns of the GIWAXS result discussed above and the previously reported value of PEA based 2D PVK.<sup>35</sup> The magnified lattice of 2D PVK also exhibits the obvious chains of [PbI<sub>6</sub>]<sup>4-</sup> octahedra and PEA<sup>+</sup> included cations. **Figure 2g** shows the EELS element mapping of each key element involved in the ETL/PVK interface of a fresh Cl<sub>6</sub>SubPc/C60 bilayer ETL based 2D/3D PVK device. We can also observe that while there are clear boundaries between other layers in the device, Cl<sub>6</sub>SubPc and C60 appear to be intermixed. The images obtained are consistent with STEM images and energy dispersive X-ray (EDX) mapping, **Supplementary Figures 9 and 10**.

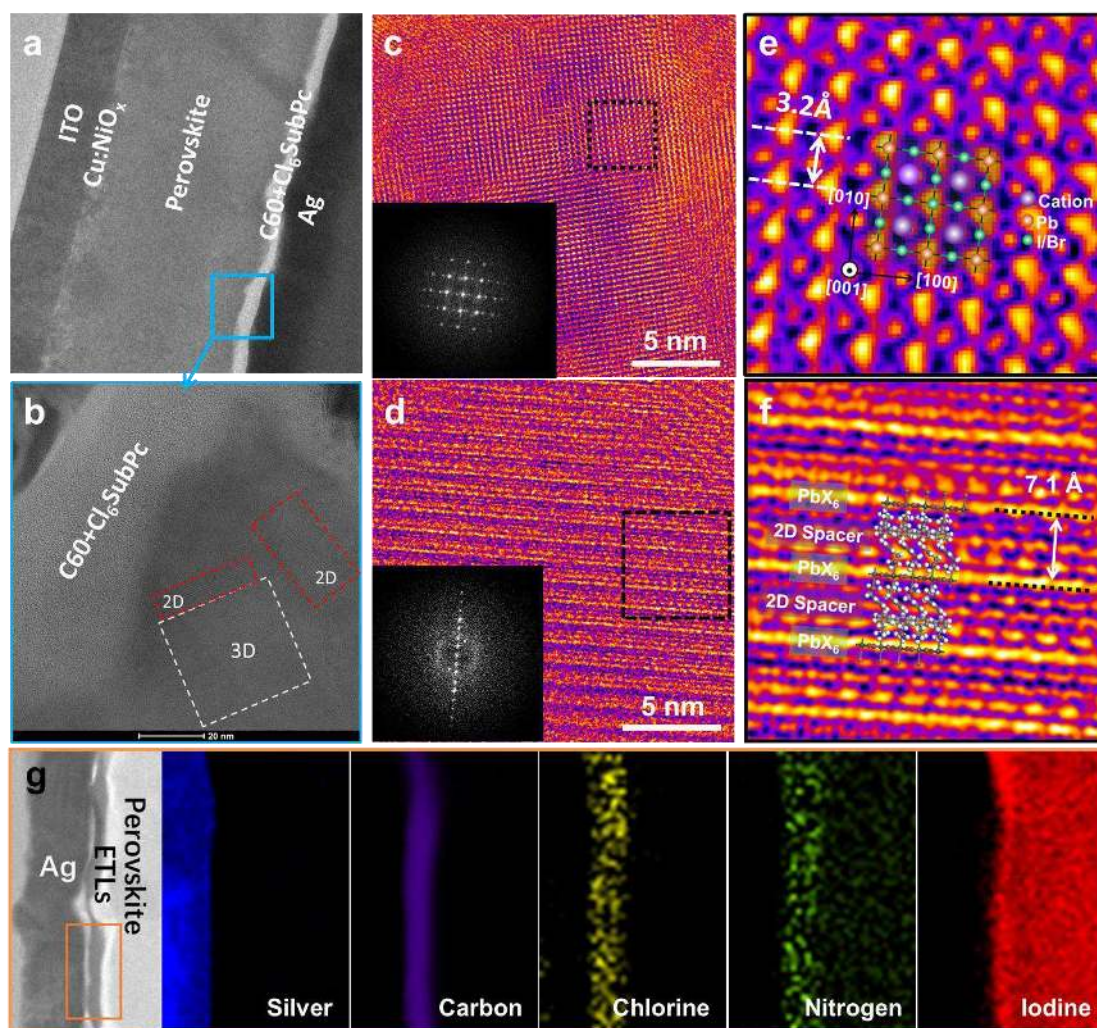


**Figure 2.** a) Cross sectional Cryo-transmission electron microscopy (TEM) image of a device with PEAI treated perovskite and Cl<sub>6</sub>SubPc/C60 ETLs; b) Cryo-TEM image of the enlarged area marked by blue frame in (a); c) Cryo-HRTEM image of the 3D region marked in (b); d) Cryo-HRTEM image of the 2D region marked in (b). Inserts in (c) and (d) are the corresponding fast Fourier transform (FFT) patterns; e) Atomic-resolution TEM image of the marked area in (c), showing 3D crystal structure of the perovskite. The inserted structural model of typical cubic lattice well matches with the TEM image; f) Atomic-resolution TEM image of the marked area in (d), showing clearly the layered structure of the 2D perovskite with interlayer distance of 7.1 Å, which is consistent with the values from the single crystal structure; g) Electron energy loss spectroscopy (EELS) mapping of the fresh devices with 3D/2D perovskite and Cl<sub>6</sub>SubPc/C60 ETLs. The Cl and N signal demonstrate that the Cl<sub>6</sub>SubPc is mixed with the C60 film.

The interactions between Cl<sub>6</sub>SubPc and perovskite could be expected from findings in a previous report on the strong chemical interactions between the copper phthalocyanine and the perovskite,<sup>37</sup> and are consistent with observed solar cell

performance improvements and improved crystallinity. Possible mechanisms of defect passivation include the formation of Pb-Cl bonds,<sup>38</sup> and the interaction between the perovskite and the pyrrole ring.<sup>37</sup> We investigated these possibilities using DFT and molecular dynamics simulations, as described in the **Supplementary Note 1**. We found that two Cl ions bond to Pb in the PbI<sub>2</sub>-terminated perovskite (001) in both possible adsorption configurations (**Supplementary Figure 11**) with a binding energy of -1.24 eV, which is much higher than the binding energy obtained for C<sub>60</sub> (-0.11 eV). The experimentally observed downward shift in the energies of the XPS peaks of Pb after Cl<sub>6</sub>SubPc deposition (**Supplementary Figure 12**) confirms the binding between the perovskite and Cl<sub>6</sub>SubPc, in agreement with a previous report on the formation of Pb-Cl bond.<sup>38</sup> In addition, we calculated the H-bonding energies for PEA-PEA cations and Cl<sub>6</sub>SubPc-PEA-Cl<sub>6</sub>SubPc (see **Supplementary Note 1**) to be -0.013 eV and -0.035 eV, respectively. Thus, the use of Cl<sub>6</sub>SubPc is expected to significantly increase the strength of interaction between the perovskite and ETL, due to hydrogen bonding (2.7 times stronger bonding with Cl<sub>6</sub>SubPc compared to hydrogen bonding between PEA molecules), Pb-Cl interactions, and the strong bonding of iodine to Cl<sub>6</sub>SubPc (more than 20 times stronger bonding with iodine compared to C<sub>60</sub>). The formation of strong bonds between the perovskite and charge transport layer are beneficial for device performance because they inhibit ion migration,<sup>1</sup> and increase resistance to degradation due to oxygen and moisture.<sup>17</sup> In addition, the existence of strong interactions between the perovskite and interfacial layer on one side, and interfacial layer and fullerene derivative on the other side was found to result in defect passivation and substantial

improvement in stability.<sup>18</sup> Interfacial bonding was confirmed to play a role in stability improvements for different molecules,<sup>37,39</sup> including copper phthalocyanine.<sup>37</sup> Thus, the stronger bonding achieved by using Cl<sub>6</sub>SubPc interfacial layer can contribute to defect passivation<sup>22</sup> and to increase the device stability.<sup>4,19,37,39</sup>

Therefore, we performed comprehensive investigation of the effects of the incorporation of Cl<sub>6</sub>SubPc on the charge recombination dynamics, the photoluminescence (PL) decay dynamics were measured to probe the interfacial recombination at the 3D/2D PVK/ETLs interfaces, followed by comprehensive stability testing. As shown in **Figure 3 a-c**, the average lifetime (samples illuminated from perovskite side) of the PVK/Cl<sub>6</sub>SubPc/C60 (626.3 ns) is similar to pure perovskites (723.5 ns), whereas the lifetime is dramatically reduced (105.9 ns) for perovskite/C60 films (**Supplementary Table 5**). No obvious differences in  $\tau_2$  lifetime are found when the samples are illuminated from the glass side. Hence, the decrease of carrier lifetime when the sample is illuminated through the ETL surface arises from interfacial recombination at the PVK/ETL interface that can be suppressed by the incorporation of Cl<sub>6</sub>SubPc ETL between 3D/2D PVK and C60.<sup>13</sup> Admittance spectroscopy was performed to determine the trap density of states (t-DOS) for the control and Cl<sub>6</sub>SubPc devices.<sup>40,41</sup> The distribution is given as  $DOS(E_\omega) = -\frac{V_{bi}}{qW} \frac{dC}{d\omega} \frac{\omega}{KT}$ , where  $V_{bi}$ ,  $W$ ,  $C$ ,  $\omega$ ,  $K$ ,  $q$  and  $T$  are built-in potential, depletion width, capacitance, angular frequency, Boltzmann constant, elementary charge and temperature, respectively.<sup>40,41</sup>  $V_{bi}$  can be obtained from the  $1/C^2$ - $V$  Mott-Schottky plots shown in **Supplementary Figure 13**, where  $V_{bi}$  is given by the intersection on the bias axis.<sup>41</sup> The trap density (**Figure 3e**)



obtained is in the range expected for a polycrystalline halide perovskite film.<sup>42</sup> We observe a reduction in the trap state density for both trap states with depths  $\sim 0.30\text{-}0.42$  eV and  $0.50\text{-}0.60$  eV in the Cl<sub>6</sub>SubPc/C<sub>60</sub> device in comparison to the C<sub>60</sub> control one by approximately one order of magnitude (for example, from  $1.53 \times 10^{17} \text{ cm}^{-3} \text{ eV}^{-1}$  to  $3.43 \times 10^{16} \text{ cm}^{-3} \text{ eV}^{-1}$  for the trap state  $\sim 0.30\text{-}0.42$  eV). We attribute these to the decrease of traps in grain boundaries and n-type interfaces, respectively,<sup>29</sup> indicating that the PVK/ETL interface quality has a significant influence on the formation of defects in the planar PSCs. The dependence of the  $V_{oc}$  on light intensity is shown in **Figure 3f**. The diode ideality factor ( $N_d$ ) can be calculated from the  $V_{oc}$  dependence on illumination intensity.<sup>43</sup>  $N_d$  is reduced from  $1.33 \text{ KT/q}$  for the C<sub>60</sub> ETLs device to  $1.12 \text{ KT/q}$  for the Cl<sub>6</sub>SubPc/C<sub>60</sub> device. A lower ideality factor indicates lower trap-assisted Shockley-Read-Hall monomolecular recombination,<sup>44,45</sup> which is consistent with the increased  $V_{oc}$ ,<sup>6</sup> lower trap densities, and the suppression of interfacial recombination for devices with Cl<sub>6</sub>SubPc/C<sub>60</sub> ETLs. From the energy levels of different materials in the devices, shown in **Figure 3**, we can observe that the electron collection would be more favorable when using C<sub>60</sub> ETL, which likely accounts for observed higher efficiency of the devices containing only C<sub>60</sub> ETL compared to only Cl<sub>6</sub>SubPc ETL.

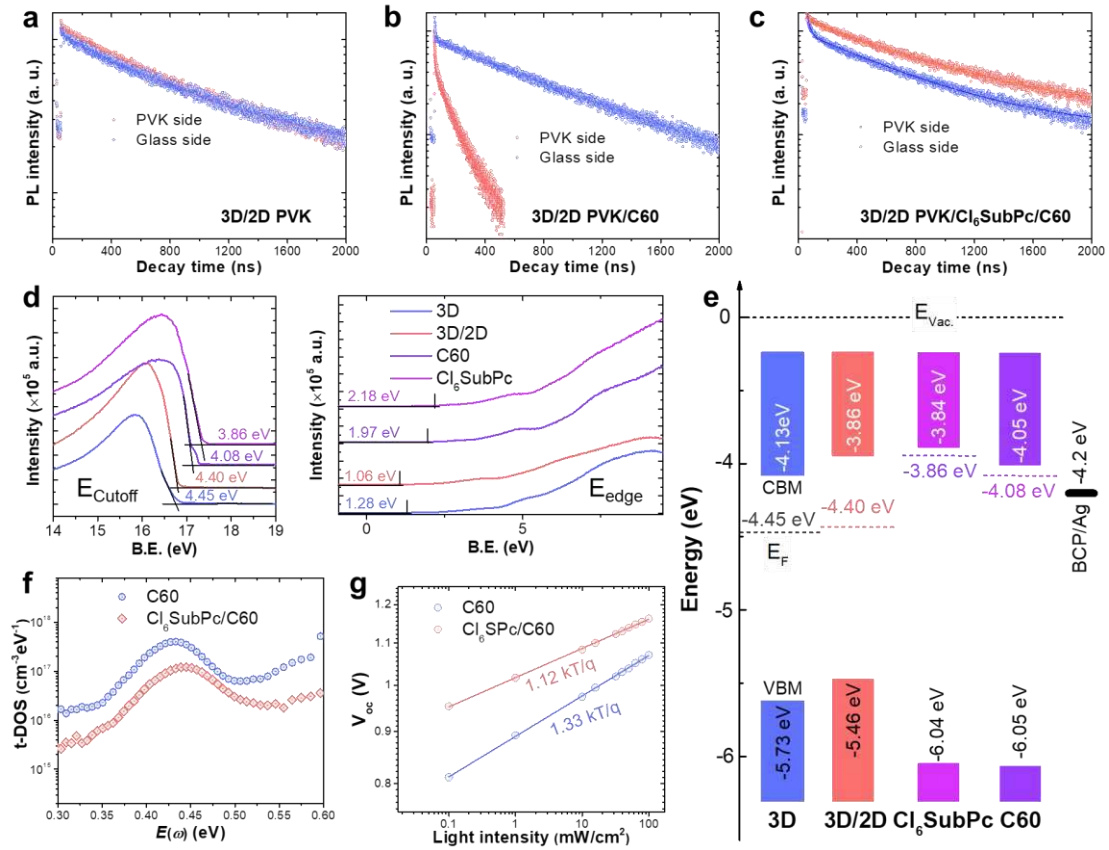


**Figure 3.** a-c) PL decay dynamics for the 3D/2D perovskites with different interlayers as noted in the figures. The excitation from glass and perovskites sides were recorded for comparison. “PVK side” indicates the excitation is from perovskite side and “Glass side” means the excitation is from glass side. d) UPS spectra for the 3D and 3D/2D perovskites as well as C60 and Cl<sub>6</sub>SubPc ETLs prepared on Si substrates; e) Energy level alignments of the various layers, the VBM, CBM and E<sub>F</sub> values were calculated from the UPS results, data for BCP/Ag were cited from literature; f) t-DOS characteristics for C60 control and Cl<sub>6</sub>SubPc/C60 ETLs based PSCs; g) Open circuit voltage (V<sub>oc</sub>) as function of illumination intensity for the C60 control and Cl<sub>6</sub>SubPc/C60 ETLs based PSCs.

After examining the charge recombination dynamics in detail, we performed comprehensive stability tests since interface degradation is a major contributor to the short and long-term PSC stability.<sup>46</sup> We performed stability tests in an inert environment to obtain information on the intrinsic stability independent of the encapsulant used.<sup>7</sup> During continuous one-sun illumination, 95% of the initial PCE is retained after 1200 hours, as shown in **Figure 4a** (corresponding time dependences of V<sub>oc</sub>, J<sub>sc</sub>, and FF are

shown in **Supplementary Figure 14**). During storage in an inert atmosphere for over 7000 hours, devices with 3D/2D perovskite passivation and Cl<sub>6</sub>SubPc/C60 ETLs maintained 99% of the initial performance, a significant improvement over devices with pure C60 ETLs, as shown in **Supplementary Figure 15**. The devices with Cl<sub>6</sub>SubPc/C60 ETLs also showed superior thermal stability with only a ~5% degradation after 2000 hours at 80 °C in a N<sub>2</sub> filled glove box, compared to ~25% obtained for devices without Cl<sub>6</sub>SubPc, as shown in **Figure 4b** (corresponding time dependences of V<sub>oc</sub>, J<sub>sc</sub>, and FF are shown in **Supplementary Figure 16**). In addition to the stability testing in inert environment, additional tests were conducted at ambient and a high temperature, high humidity (85°C, 85% RH) environment, using encapsulated devices (schematic diagrams are shown in **Supplementary Figures 17 and 18**). We also observe a superior performance in damp heat test, where devices with Cl<sub>6</sub>SubPc/C60 ETLs exhibit T<sub>80</sub> of 816 h (34 days), while devices with C60 ETLs drop below 80% of initial efficiency within the first day of testing, as shown in **Figure 4c**. We also performed outdoor testing since outdoor stability studies of PSCs in general have been scarce,<sup>7</sup> and there have been no outdoor tests of inverted devices to date. Superior stability of the devices with Cl<sub>6</sub>SubPc/C60 ETLs compared to C60 ETLs is also confirmed in outdoor stability tests following ISOS-O1 protocol, where T<sub>95</sub> of 1272h for device with Cl<sub>6</sub>SubPc is obtained, as shown in **Figure 4d**. The encapsulated cell with Cl<sub>6</sub>SubPc/C60 ETL exhibited excellent stability in ambient under simulated solar illumination and MPP tracking, as shown in **Figure 4e**.

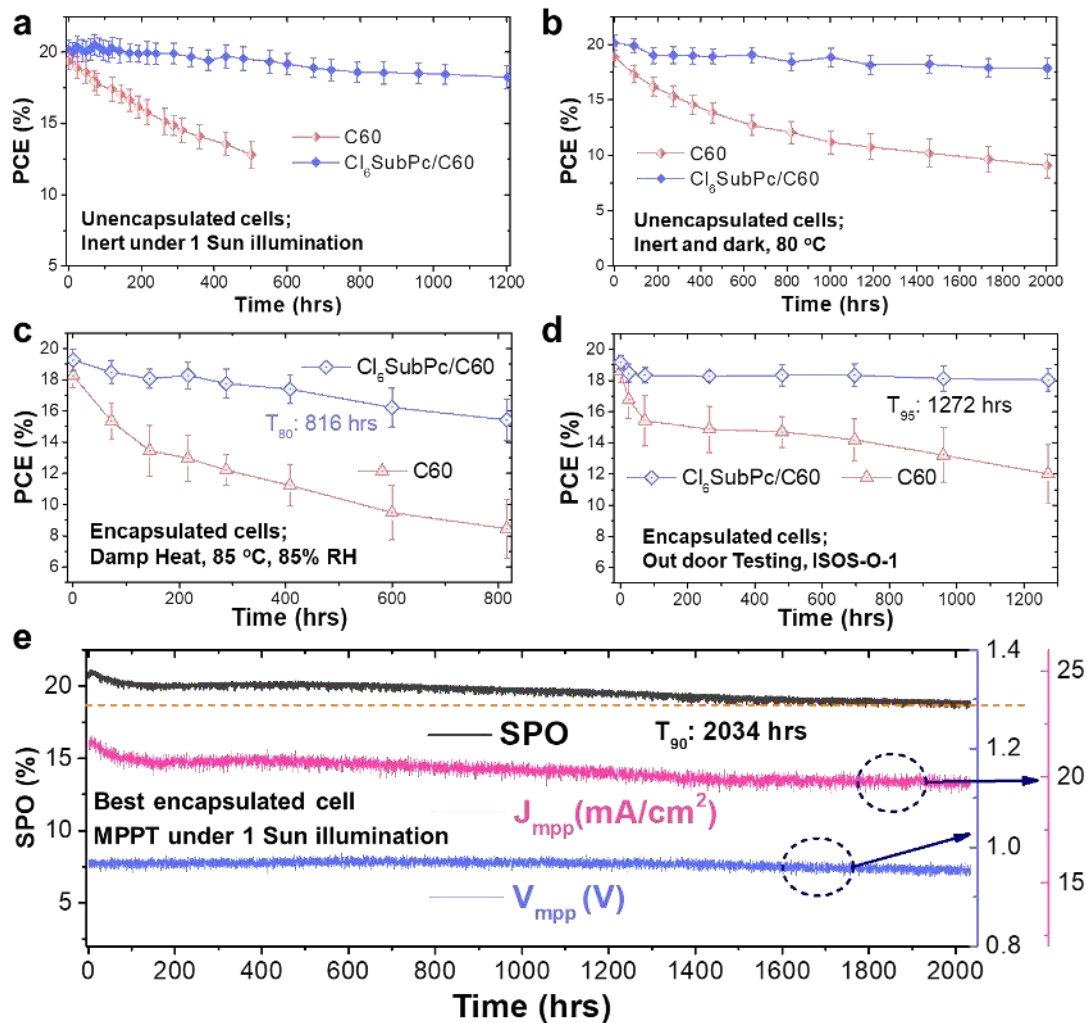


**Figure 4.** a) Light stability tests of the control C60 devices (6 cells) and Cl<sub>6</sub>SubPc/C60 devices (6 cells) in inert atmosphere. The devices were un-encapsulated, and the I-V curves were recorded at certain time intervals; b) Thermal stability tests of the control C60 devices (6 cells) and Cl<sub>6</sub>SubPc/C60 devices (8 cells) at 80 °C under inert and dark environment; c) Damp heat stability tests of the encapsulated control C60 devices (5 cells) and Cl<sub>6</sub>SubPc/C60 devices (5 cells); d) Outdoor stability tests of the encapsulated control C60 devices (5 cells) and Cl<sub>6</sub>SubPc/C60 devices (9 cells) following the ISOS-O-1 protocol standard; e) Light stability of encapsulated Cl<sub>6</sub>SubPc/C60 cell in ambient under continuous 1 sun illumination and maximum power point tracking (MPPT).

It should be noted that all the stability tests were performed on devices with 3D/2D PVK layers. Since it has been reported that bulky organic cations in the 2D PVK structure of the 3D/2D PVK capping layers improves device stability by inhibiting ion migration,<sup>8,30,47,48</sup> we also compared the stability of devices with 3D and 3D/2D PVK

and C60 ETL, as shown in **Supplementary Figure 19**. Thus, we can observe that while 3D/2D PVK results in improved stability compared to 3D PVK active layer, as expected,<sup>8,30,35,47,48</sup> it is not sufficient to enable significant performance improvement under realistic operating conditions. From the comparison of the stability of the devices with 3D PVK active layer and Cl<sub>6</sub>SubPc/C60 and C60-only ETLs, as shown in **Supplementary Figure 20**. We see that the stability of the devices with 3D PVK and Cl<sub>6</sub>SubPc/C60 is clearly better than that of 3D PVK and C60-only. Thus, we focus on the effect of the PVK/ETL interface on device stability in devices with 3D/2D perovskite and Cl<sub>6</sub>SubPc/C60 bilayer ETL.

In addition to stability tests at elevated temperature, humidity and/or illumination, we performed stability testing under reverse bias, since this type of test is a strong indicator of susceptibility to ion migration and electrode corrosion.<sup>16,17</sup> To further enhance susceptibility to ion migration, the devices were illuminated during testing, since illumination and electrical bias both promote ion and defect migration, and accelerate harmful chemical reactions.<sup>7</sup> In the device without Cl<sub>6</sub>SubPc (**Supplementary Figure 21**) we can see clear damage to the Ag electrode, and also Ag deposition on the ITO side, in agreement with the literature,<sup>16</sup> while in the devices with Cl<sub>6</sub>SubPc/C60 (**Supplementary Figure 22**) no obvious electrode damage can be seen, confirming further that Cl<sub>6</sub>SubPc is capable of blocking ion migration.

To investigate the mechanism behind the effect of Cl<sub>6</sub>SubPc in device stability tested above, we performed ToF-SIMS, EELS mapping, and XPS measurements on devices with different ETLs. From obtained SIMS profiles (**Figure 5 a and b**, and

**Supplementary Figure 23**) of the C60-only and Cl<sub>6</sub>SubPc/C60 devices before and after aging, we observe the iodine at the initial sputtering atmosphere of the aged C60-only device in contrast to the fresh one, along with the variation of silver information. In contrast, the Cl<sub>6</sub>SubPc/C60 device shows negligible change in those profiles. Information on other key elements or species involved in the devices before and after aging are also shown in **Supplementary Figure 23**. To verify the profiles obtained from SIMS and provide direct visual evidence of ion migration, we have applied our successful experience of sample preparation and HRTEM-characterization of the intact device cross-section, and obtained visual EELS mappings of involved key elements of fresh and aged devices. **Figure 5c-d** show the EELS mappings of the aged device cross-sections of the C60-only and Cl<sub>6</sub>SubPc/C60 device, compared with those of the corresponding fresh one (**Figure 2g** and **Supplementary Figure 24**). The iodine mapping in the aged C60-only device proves unambiguously the existence of iodide inside the silver electrode, while the counterpart iodine mapping in the aged Cl<sub>6</sub>SubPc/C60 device shows negligible existence of iodine in the corresponding silver electrode layer. This contrast reveals in a direct view the effect of Cl<sub>6</sub>SubPc to block the migration of iodine ions although that is well known already.

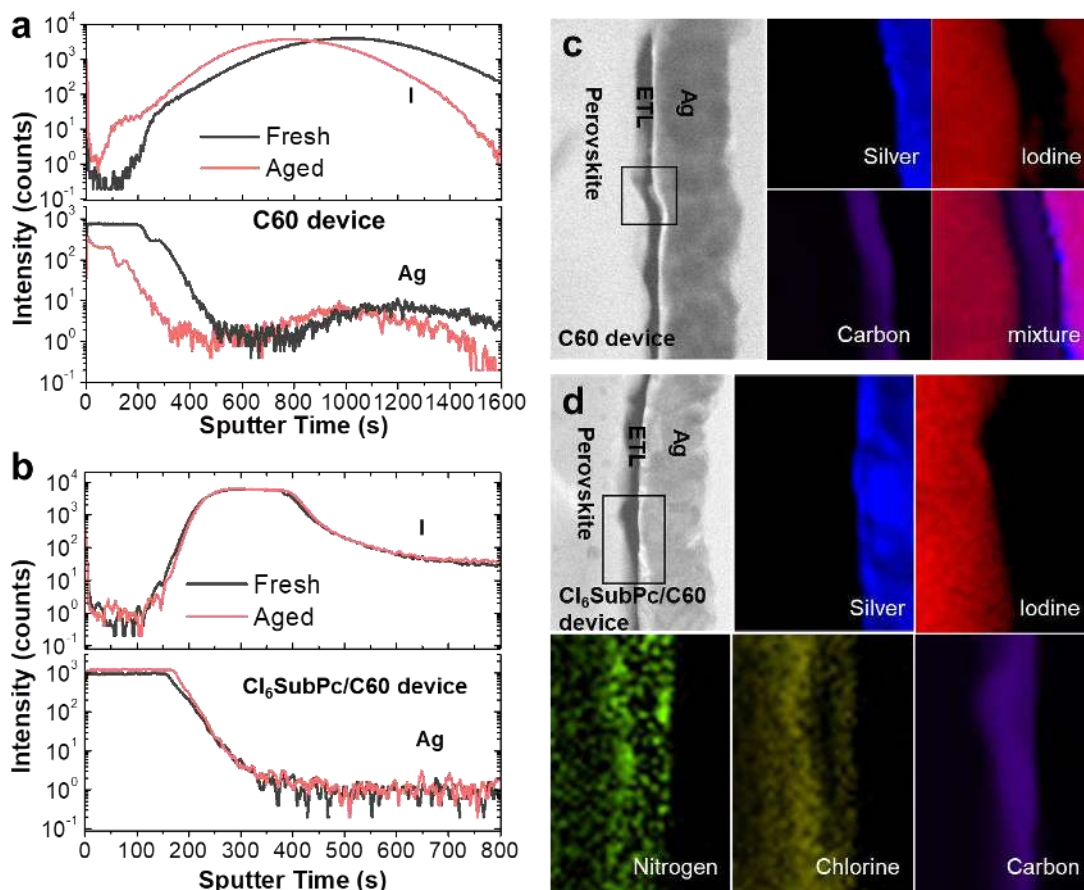


**Figure 5.** a) and b) Secondary-ion mass spectrometry (SIMS) profiles of I<sup>-</sup> and Ag<sup>+</sup> ions for the C60 control device (a) and Cl<sub>6</sub>SubPc/C60 device (b) before and after aging; c) and d) lateral EELS mapping of the aged C60 control device (c) and Cl<sub>6</sub>SubPc/C60 (d) device.

Moreover, in agreement with the SIMS and EELS mapping results, XPS spectra of the devices with Cl<sub>6</sub>SubPc/C60 ETL do not show significant changes in the I and Ag spectra after aging, different from devices with C60 ETLs, as shown in **Supplementary Figure 25**. Surface potential scans probed by scanning Kelvin probe microscopy (SKPM) further highlight the differences in the stability of the PVK/ETL interface with and without Cl<sub>6</sub>SubPc (**Supplementary Figures 26 and 27**). The surface potential for the perovskite with Cl<sub>6</sub>SubPc/C60 ETLs, showed no obvious changes as function of illumination (continuous light soaking with a white LED lamp, ~40 mA/cm<sup>2</sup>) (**Supplementary Figure 27**), while perceptible changes have been observed in the

C60-only sample (**Supplementary Figure 26**). The demonstrated improvement in the device stability and the stability of the Cl<sub>6</sub>SubPc/PVK interface that hinders the ion migration is in agreement with the calculated binding energy for iodine ions (-0.43 eV for Cl<sub>6</sub>SubPc and -0.019 eV for C60), since the binding energy increase would stabilize the PVK/ETL interface (**Supplementary note S1**).

To further investigate the reason of the blocking effect of Cl<sub>6</sub>SubPc, XPS spectra of Cl<sub>6</sub>SubPc film treated with iodide vapor were measured, as shown in **Supplementary Figure 28**. The I<sup>-</sup> signal can be detected in the treated film and the binding energy of N 1s core was shifted to a lower energy, indicating a strong interaction between N and I.<sup>49</sup> The N in the Cl<sub>6</sub>SubPc contributes to I<sup>-</sup> adsorption, which suppresses ion migration in the PVK/ETL interface. This is in agreement with the known capability of macrocyclic molecules (porphyrins, phthalocyanines) to effectively adsorb iodine,<sup>26</sup> as well as the high iodide ion binding energy of the Cl<sub>6</sub>SubPc. In addition to interactions between N and I, boron atom can also contribute to the interactions with the perovskite, since we observed an obvious red shift of the binding energy of B1s from 191 to 186 eV, as shown in **Supplementary Figure 29b**. This shift is consistent with electron transfer, which likely occurs due to high electron affinity of boron, similar to a previous report of electron transfer between SubPc and C60, which also resulted in a similar shift of the B 1s peak.<sup>50</sup> Consequently, Cl<sub>6</sub>SubPc strongly interacts with both perovskite, as evidenced by XPS results shown in **Supplementary Figure 29b**, and C60 based on literature reports,<sup>50</sup> and this can contribute to the stabilization of the interface<sup>37,39</sup> as well as improved charge



collection.<sup>18</sup> It should be noted that this electron transfer can result in the possible loss of axial chlorine, which could then diffuse into the perovskite layer and hence be detected in the perovskite layer after aging, as shown in EELS mapping images, **Figure 5d**. That may also correlate to a small shift in Cl profile in the SIMS profiles (**Supplementary Figure 23**). As discussed above, the synergistic effect of N, B and Cl elements of Cl<sub>6</sub>SubPc accounts for the correlated chemical bonding with both PVK and C60, leading to the effective suppression of ions migration at the interface.

Finally, to examine the validity and general applicability of phthalocyanine molecule structure in enhancing device stability, a typical electron-transport molecule, F<sub>16</sub>CuPc whose structure is shown in **Supplementary Figure 30a**, was tested as a replacement for Cl<sub>6</sub>SubPc in device structure. The devices with F<sub>16</sub>CuPc/C60 ETLs exhibit much lower efficiency of 16.39%, as shown in **Supplementary Figure 30b**. The inferior performance compared to Cl<sub>6</sub>SubPc/C60 devices can be attributed to unfavorable energy level alignment, as shown in **Supplementary Figure 31**, and consistent with the observed lower FF (due to the increase of series resistance), which indicates less efficient charge collection. In contrast to the control C60-only device, the devices with F<sub>16</sub>CuPc/C60 still exhibit superior stability under illumination and MPPT (**Supplementary Figure 32**), as well as reverse bias and illumination (**Supplementary Figure 33**), similar as the devices with Cl<sub>6</sub>SubPc/C60 ETL. This result further demonstrates that the phthalocyanines can effectively interact with iodine and the perovskite and thus inhibit the ion migration.

In summary, we have shown that the Cl<sub>6</sub>SubPc/C60 combined ETL can dramatically boost the device stability, as well as improve the conversion efficiency owing to the unique properties of Cl<sub>6</sub>SubPc. Based on comprehensive experimental characterizations and theoretical simulations, N and B atoms of Cl<sub>6</sub>SubPc could have obvious chemical bonding with migrated halide ions from perovskites, which in addition to Pb-Cl bonds results in strong interactions between the ETL and perovskite, resulting in effective inhibition of the halide ion migration at the ETL/PVK interface and the suppression of electrode corrosion, as evidenced by EELS mapping, TOF-SIMS, and XPS. As a result of effective interfacial management strategy, we obtained inverted planar PSCs with high conversion efficiency of 22 % (21.3% certified) and unprecedented long-term stability (95% of PCE retained over 1200h of outdoor testing and 90% of PCE retained under illumination and MPPT for over 2000 h). This strategy can be extended to extensive phthalocyanines with suitable electronic structures for interfacial stabilization of PSCs. Our results highlight multilayer ETLs incorporating halogenated macrocyclic molecules as a promising route for both high performance and stable perovskite solar cells.

**Data availability.** The data that support the plots within this paper and other findings of this study are available from the corresponding authors upon reasonable request.

## **Acknowledgements**

This work is supported by the National Natural Science Foundation of China (NSFC) (No. 61775091), the Shenzhen Key Laboratory Project (No. ZDSYS201602261933302) and Natural Science Foundation of Shenzhen Innovation Committee (Nos. JCYJ20180504165851864, JCYJ20170818141216288). A. B. D. would like to

acknowledge support of Seed Funding for Basic Research and Seed Funding for Strategic Interdisciplinary Research Scheme of the University of Hong Kong and Shenzhen Science and Technology Commission Projects No. JCYJ20170818141216288. The authors thank the Core Research Facilities (CRF) and the Pico Center of SUSTech for some characterizations in this work. Q. H. and T. P. R. were supported by the US Office of Naval Research under contract N00014-17-1-2241. GIXD were performed at beamline 7.3.3 at Advanced Light Source, Lawrence Berkeley National Laboratory, which was supported by the DOE, Office of Science, and Office of Basic Energy Sciences.

### **Author contributions**

Z.H., A.B.D, and T. P. R. conceived and supervised the project. W. C., Q. H., R. Z., T. P. R., A.B.D, and Z.H. wrote the paper. W.C. fabricated and characterized the perovskite solar cells. Q. H., W. Y. and performed GIWAXS measurements and analyzed the GIWAXS data. YD. Z., B. H., W. C. and M. G. finished the FIB, STEM, EELS and HRTEM characteristics. R. Cheng and S. P. F. performed damp heat stability tests. YC. Z performed the theoretical calculation and analyzed the results. B. T., D. L., F. Z. L. and YD. Z. helped perform all other related characteristics and measurements. All authors discussed and analyzed the results.

### **Competing interests**

The authors declare no competing interests.

### **Additional information**

**Supplementary information** is available for this paper at <https://xxxx>.

**Reprints and permissions information** is available at [www.nature.com/reprints](http://www.nature.com/reprints).

**Correspondence and requests for materials** should be addressed to Z.H. [hezbs@sustech.edu.cn](mailto:hezbs@sustech.edu.cn); A.B.D. [dalek@hku.hk](mailto:dalek@hku.hk); or T. P. R. [russel@mail.pse.umass.edu](mailto:russel@mail.pse.umass.edu)

**Publisher's note:** Springer Nature remains neutral with regard to jurisdictional claims in published maps and institutional affiliations.

### **References**

1. National Renewable Energy Laboratory, Best research-cell efficiencies, Accessed,

August, 2020.

2. Min H. *et al.* Efficient, stable solar cells by using inherent bandgap of  $\alpha$ -phase formamidinium lead iodide. *Science* 366, 749-753 (2019)
3. Zheng, X. P. *et al.* Managing grains and interfaces via ligand anchoring enables 22.3%-efficiency inverted perovskite solar cells. *Nat. Energy* 5, 131-140, (2020).
4. Roose, B. *et al.* The role of charge selective contacts in perovskite solar cell stability. *Adv. Energy Mater.*, 2019, 9, 1803140.
5. Rong, Y. *et al.* Challenges for commercializing perovskite solar cells. *Science* 361, eaat8235 (2018).
6. Luo, D. *et al.* Enhanced photovoltage for inverted planar heterojunction perovskite solar cells. *Science* 360, 1442-1446 (2018).
7. Khenkin, M. V. *et al.* Consensus statement for stability assessment and reporting for perovskite photovoltaics based on ISOS procedures. *Nat. Energy*, 5, 35-49 (2020).
8. Boyd, C. C. *et al.* Understanding degradation mechanisms and improving stability of perovskite photovoltaics. *Chem. Rev.* 119, 3418-3451 (2019).
9. Zhao, X. *et al.* Effect of selective contacts on the thermal stability of perovskite solar cells. *ACS Appl. Mater. Interfaces* 9, 7148-7153 (2017).
10. Bai, S. *et al.* Planar perovskite solar cells with long-term stability using ionic liquid additives. *Nature* 571, 245-250 (2019).
11. Checharoen, R. *et al.* Design and understanding of encapsulated perovskite solar cells to withstand temperature cycling. *Energy Environ. Sci.* 11, 144-150 (2018).
12. Bowring, A. R. *et al.* Reverse bias behavior of halide perovskite solar cells. *Adv. Energy Mater.* 8, 1702365, (2018).
13. Stolterfoht, M. *et al.* Visualization and suppression of interfacial recombination for high-efficiency large-area pin perovskite solar cells. *Nat. Energy* 3, 847-854 (2018).
14. Lian, J., *et al.* Electron-transport materials in perovskite solar cells. *Small Methods* 2, 1800082 (2018).
15. Akbulatov, A. F. *et al.* Effect of Electron-Transport Material on Light-Induced Degradation of Inverted Planar Junction Perovskite Solar Cells. *Adv. Energy Mater.* 7, 1700476 (2017).
16. Razera, R. A. Z. *et al.* Instability of p-i-n perovskite solar cells under reverse bias. *J. Mater. Chem. A* 8, 242-250, (2020).
17. Yang, S. *et al.* Stabilizing halide perovskite surfaces for solar cell operation with wide-bandgap lead oxysalts. *Science* 365, 473-478 (2019).
18. Zou, M. H. *et al.* Strengthened perovskite/fullerene interface enhances efficiency and stability of inverted planar perovskite solar cells via a tetrafluoroterephthalic acid interlayer. *ACS Appl. Mater. Interfaces* 11, 33515-33524, (2019).
19. Huang, Z. Q. *et al.* Water-resistant and flexible perovskite solar cells via a glued interfacial layer. *Adv. Funct. Mater.* 29, 1902629, (2019).
20. Wang, H. L. *et al.* Efficient surface passivation and electron transport enable low temperature-processed inverted perovskite solar cells with efficiency over 20%. *ACS Sustainable Chem. Eng.* 8, 8845-8856, (2020).
21. Zheng, T. *et al.* Engineering of electron extraction and defect passivation via anion-doped conductive fullerene derivatives as interlayers for efficient invert perovskite

- solar cells. *ACS Appl. Mater. Interface* 12, 24747-24755, (2020).
22. Xue, Q. F. *et al.* Dual interfacial modifications enable high performance semitransparent perovskite solar cells with large open circuit voltage and fill factor. *Adv. Energy Mater.* 7, 1602333 (2017).
  23. Urbani, M., *et al.* Phthalocyanines and porphyrinoid analogues as hole- and electron-transporting materials for perovskite solar cells, *Chem. Soc. Rev.* 48, 2738-2766, (2019).
  24. Duan, C. *et al.* The role of the axial substituent in subphthalocyanine acceptors for alk-heterojunction solar cells. *Angew. Chem. Int. Ed.* 56, 148-152 (2017).
  25. Lee, H. *et al.* Interfacial electronic structure of Cl<sub>6</sub>SubPc non-fullerene acceptors in organic photovoltaics using soft X-ray spectroscopies. *Phys. Chem. Chem. Phys.* 19, 31628-31633, (2017).
  26. Li, H., *et al.* Porous azo-bridged porphyrin-phthalocyanine network with high iodine capture capability. *Chem.* 22, 11863-11868 (2016).
  27. Chen, W. *et al.* Understanding the doping effect on NiO: toward high-performance inverted perovskite solar cells. *Adv. Energy Mater.* 8, 1703519 (2018).
  28. Saliba, M. *et al.* Cesium-containing triple cation perovskite solar cells: improved stability, reproducibility and high efficiency. *Energy Environ. Sci.* 9, 1989-1997 (2016).
  29. Chen, W. *et al.* Alkali chlorides for the suppression of the interfacial recombination in inverted planar perovskite solar cells. *Adv. Energy Mater.* 9, 1803872 (2019).
  30. Bai, Y. *et al.* Dimensional engineering of a graded 3D-2D halide perovskite interface enables ultrahigh V<sub>oc</sub> enhanced stability in the p-i-n photovoltaics. *Adv. Energy Mater.* 7, 1701038 (2017).
  31. Quan, L. N. *et al.* Ligand-stabilized reduced-dimensionality perovskites. *J. Am. Chem. Soc.* 138, 2649-2655 (2016).
  32. Quintero-Bermudez, R. *et al.* Compositional and orientational control in metal halide perovskites of reduced dimensionality. *Nat. Mater.* 17, 900-907 (2018).
  33. Xue, J. *et al.* Crystalline liquid-like behavior: surface-induced secondary grain growth of photovoltaic perovskite thin film. *J. Am. Chem. Soc.* 141, 13948-13953 (2019).
  34. Chen, J. *et al.* MAPbI<sub>3</sub> self-recrystallization induced performance improvement for oxygen-containing functional groups decorated carbon nanotube-based perovskite solar cells. *Solar RRL* 3, 1900302, (2019).
  35. J. W. Lee *et al.* 2D perovskite stabilized phase-pure formamidinium perovskite solar cells, *Nature Comm.* 9, 3021 (2018).
  36. Y. M. Zhu *et al.* Direct atomic scale characterization of the surface structure and planar defects in the organic-inorganic hybrid CH<sub>3</sub>NH<sub>3</sub>PbI<sub>3</sub> by Cryo-TEM, *Nano Energy* 73, 104820, (2020).
  37. Kim, Y. C. *et al.* Engineering interface structures between lead halide perovskite and copper phthalocyanine for efficient and stable perovskite solar cells. *Energy Environ. Sci.* 10, 2109-2116, (2017).
  38. Wang, Y. *et al.* Stabilizing heterostructures of soft perovskite semiconductors. *Science* 365, 687-691 (2019).
  39. Luo, B. C. *et al.* Interfacial bonding and electronic structure between thiocyanate

and hybrid organohalide lead perovskites for photovoltaic application. *J. Phys. Chem. Lett.* 10, 5609-5616, 2019.

40. Khadka, D. B. *et al.* Unraveling the impacts induced by organic and inorganic hole transport layers in inverted halide perovskite solar cells. *ACS Appl. Mater. Interfaces* 11, 7055-7065 (2019).

41. Wang, Q. *et al.* Large fill-factor bilayer iodine perovskite solar cells fabricated by a low-temperature solution-process. *Energy Environ. Sci.* 7, 2359 (2014).

42. Shao, Y. *et al.* Origin and elimination of photocurrent hysteresis by fullerene passivation in  $\text{CH}_3\text{NH}_3\text{PbI}_3$  planar heterojunction solar cells. *Nat. Comm.* 5, 5784 (2014).

43. Tress, W. *et al.* Interpretation and evolution of open-circuit voltage, recombination, ideality factor and subgap defect states during reversible light-soaking and irreversible degradation of perovskite solar cells. *Energy Environ. Sci.* 11, 151-165 (2018).

44. Li, Z. *et al.* Controlled surface decomposition derived passivation and energy-level alignment behaviors for high performance perovskite solar cells. *J. Mater. Chem. A* 6, 9397-9401 (2018).

45. Chen, W. *et al.* Molecule-doped nickel oxide: verified charge transfer and planar inverted mixed cation perovskite solar cell. *Adv. Mater.* 30, 1800515 (2018).

46. Brinkmann, K. O. *et al.* Suppressed decomposition of organometal halide perovskites by impermeable electron-extraction layers in inverted solar cells. *Nat. Comm.* 8, 13938 (2017).

47. Chen, P. *et al.* In situ growth of 2D perovskite capping layer for stable and efficient perovskite solar cells. *Adv. Funct. Mater.* 28, 1706923 (2018).

48. Grancini, G. *et al.* One-year stable perovskite solar cells by 2D/3D interface engineering. *Nat. Comm.* 8, 15684 (2017).

49. Back, H. *et al.* Achieving long-term stable perovskite solar cells via ion neutralization. *Energy Environ. Sci.* 9, 1258-1263 (2016).

50. Lo, M. F. *et al.* Suppression of time-dependent donor/acceptor interface degradation by redistributing donor charge density. *Adv. Mater. Interfaces* 1, 1300082, (2014).

# Figures

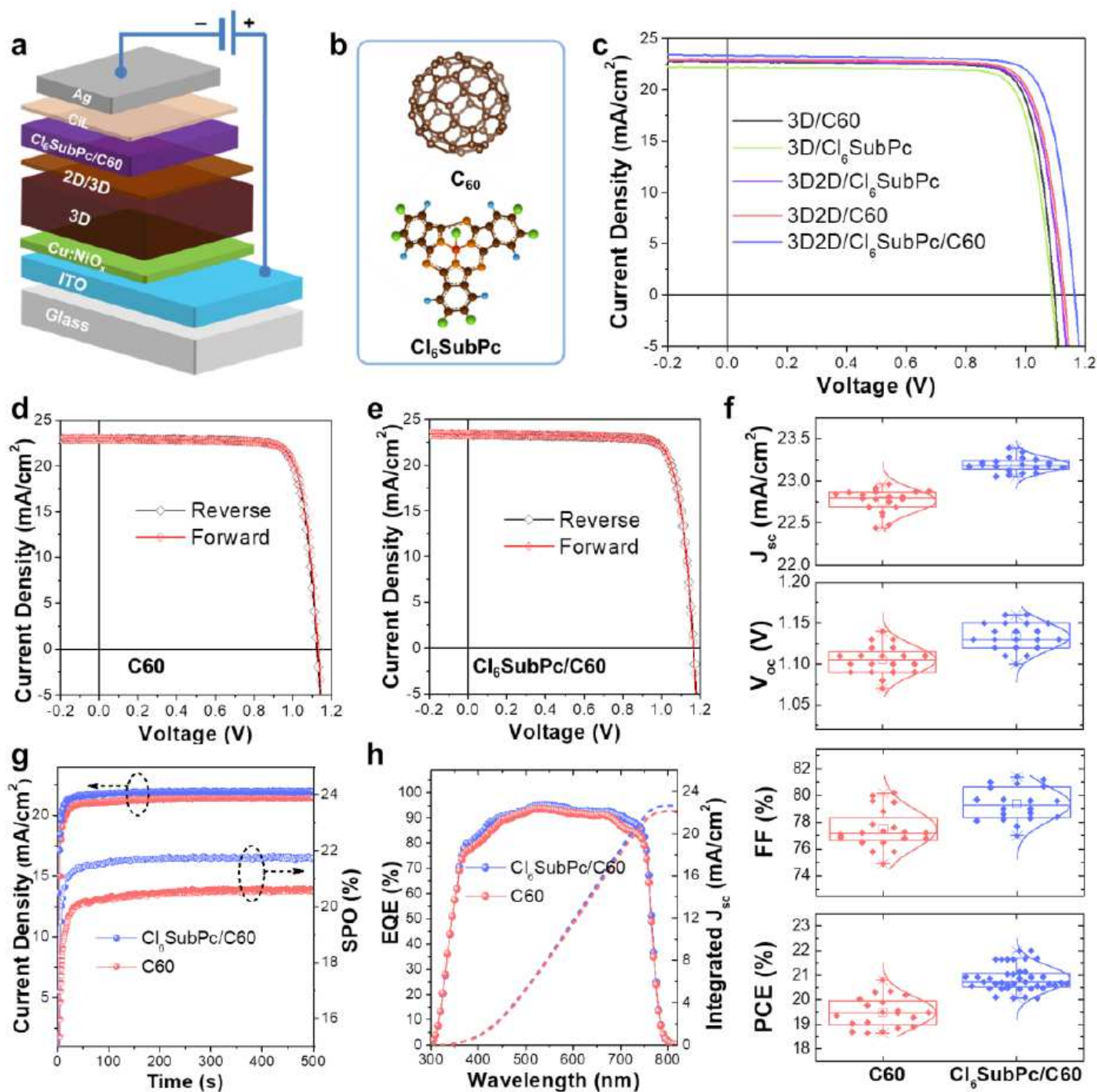
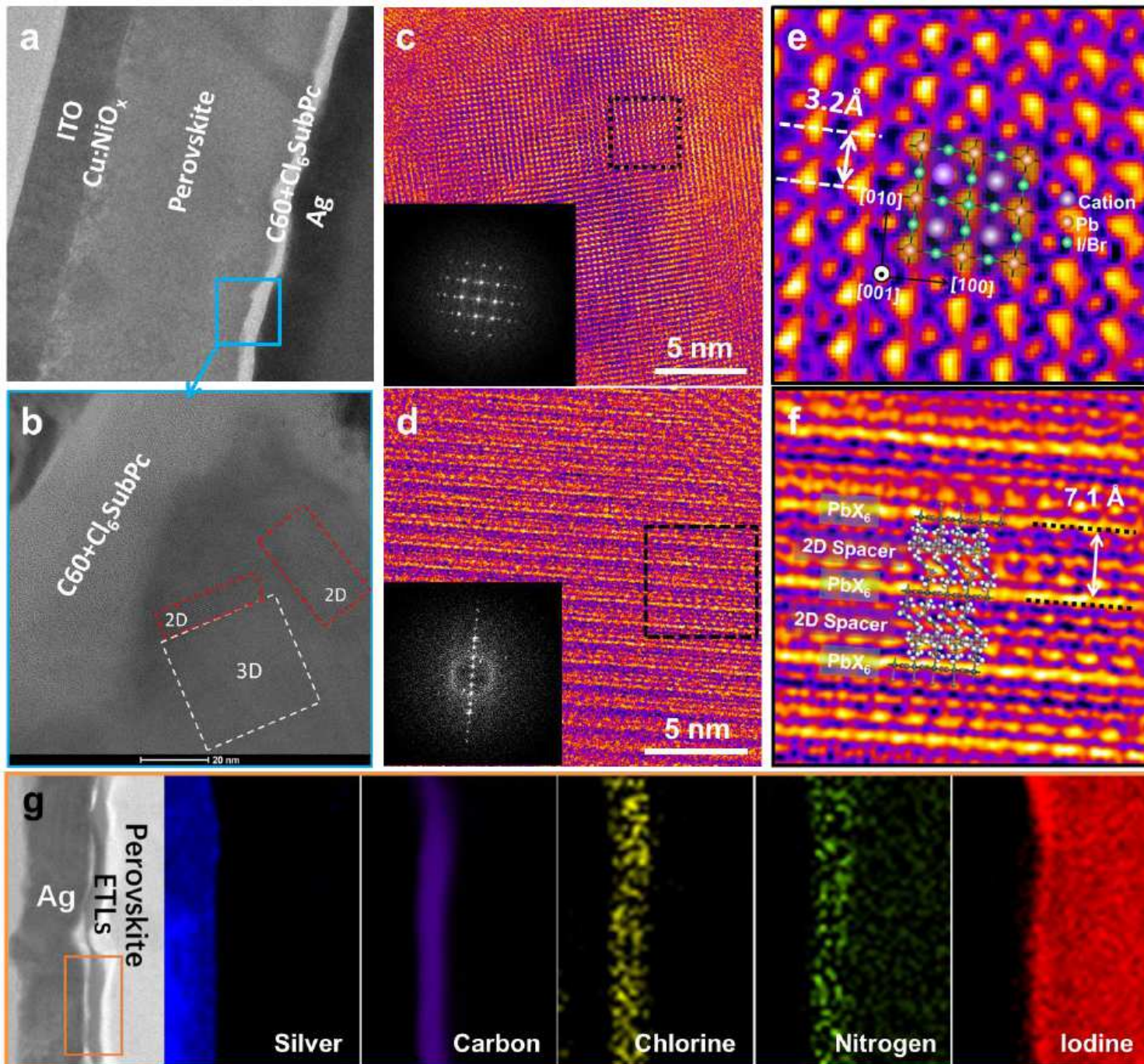


Figure 1

a) Device architecture of the inverted planar perovskite solar cells (PSCs); b) Molecular structures of the  $\text{C}_{60}$  and chlorinated macrocyclic molecule ( $\text{Cl}_6\text{SubPc}$ ) ETLs; c) J-V curves of the PSCs with various ETLs (reverse scan) under 1 sun illumination; d-e) J-V curves of the optimal 3D/2D/C60 (d) and 3D/2D/ $\text{Cl}_6\text{SubPc/C60}$  (e) devices under reverse and forward scan directions; f) Device performance statistics for 3D/2D/C60 and 3D/2D/ $\text{Cl}_6\text{SubPc/C60}$  devices; g) Steady power output (SPO) of the

optimal 3D/2D/C60 and 3D/2D/Cl6SubPc/C60 devices test at the bias of maximum power point; h) EQE spectra for the optimal 3D/2D/C60 and 3D/2D/Cl6SubPc/C60 devices.

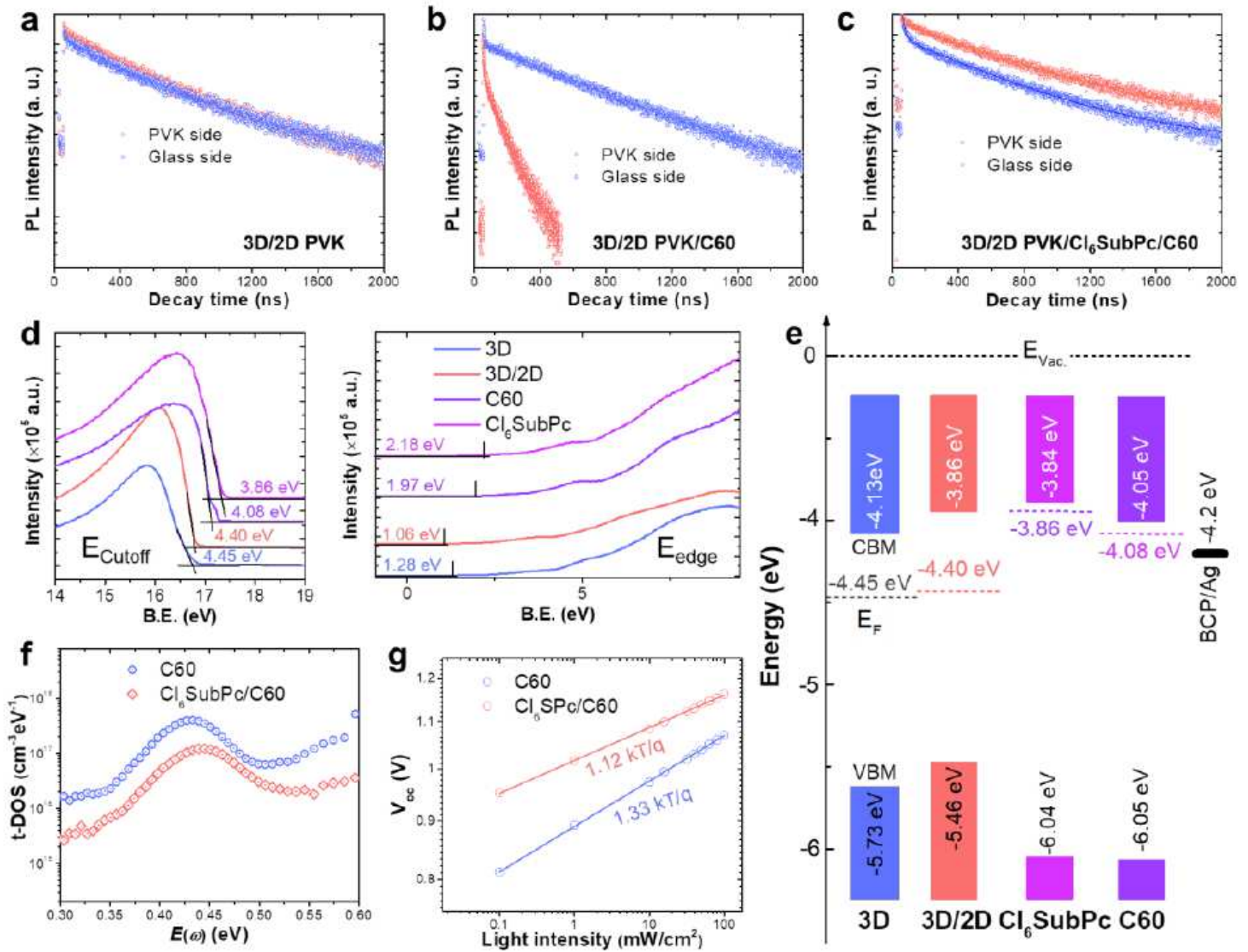


**Figure 2**

a) Cross sectional Cryo-transmission electron microscopy (TEM) image of a device with PEAI treated perovskite and Cl6SubPc/C60 ETLs; b) Cryo-TEM image of the enlarged area marked by blue frame in (a); c) Cryo-HRTEM image of the 3D region marked in (b); d) Cryo-HRTEM image of the 2D region marked in (b). Inserts in (c) and (d) are the corresponding fast Fourier transform (FFT) patterns; e) Atomic-resolution TEM image of the marked area in (c), showing 3D crystal structure of the perovskite. The inserted structural model of typical cubic lattice well matches with the TEM image; f) Atomic-resolution TEM

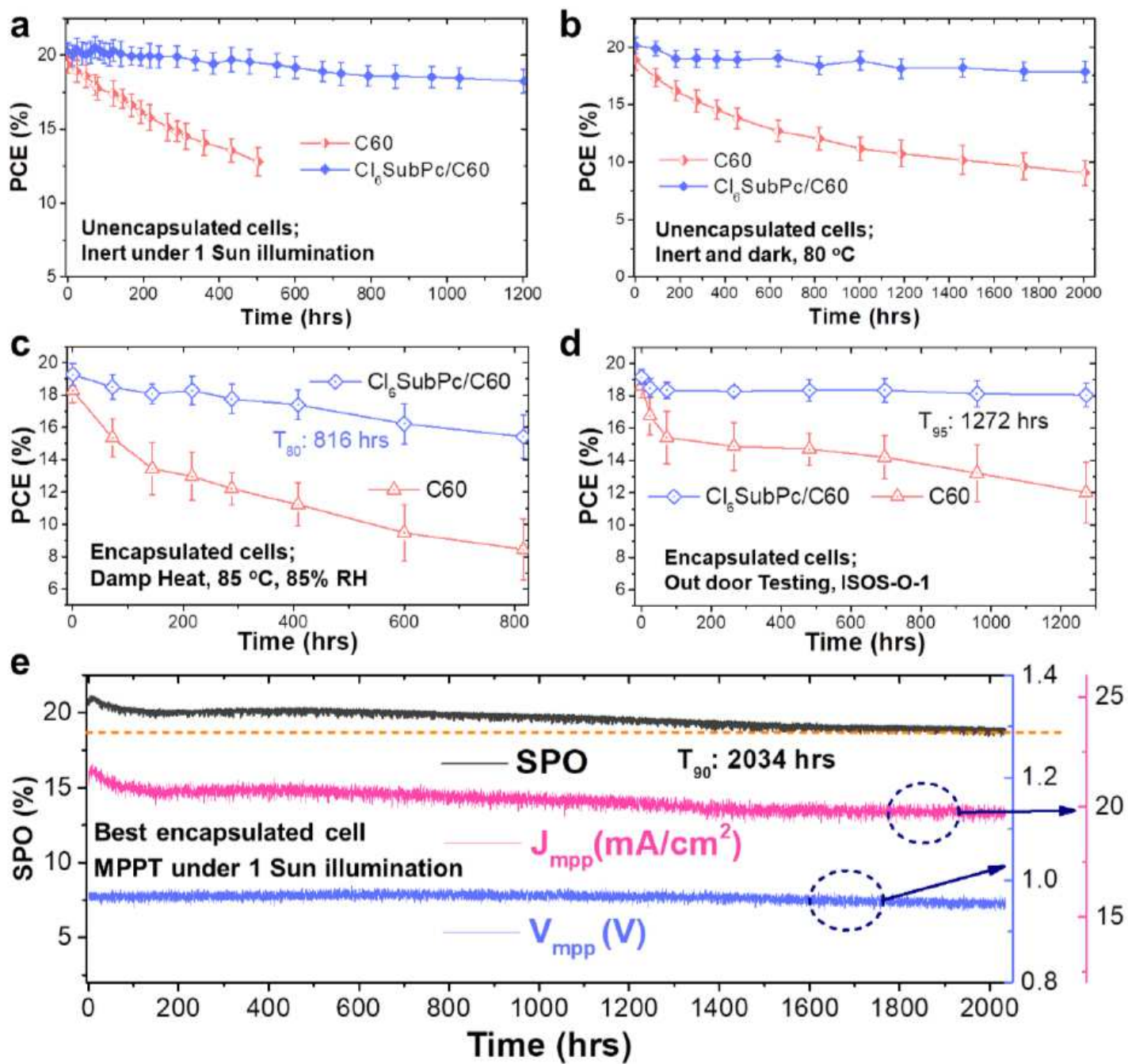


image of the marked area in (d), showing clearly the layered structure of the 2D perovskite with interlayer distance of  $7.1\text{\AA}$ , which is consistent with the values from the single crystal structure; g) Electron energy loss spectroscopy (EELS) mapping of the fresh devices with 3D/2D perovskite and Cl<sub>6</sub>SubPc/C60 ETLs. The Cl and N signal demonstrate that the Cl<sub>6</sub>SubPc is mixed with the C60 film.



**Figure 3**

a-c) PL decay dynamics for the 3D/2D perovskites with different interlayers as noted in the figures. The excitation from glass and perovskites sides were recorded for comparison. “PVK side” indicates the excitation is from perovskite side and “Glass side” means the excitation is from glass side. d) UPS spectra for the 3D and 3D/2D perovskites as well as C60 and Cl<sub>6</sub>SubPc ETLs prepared on Si substrates; e) Energy level alignments of the various layers, the VBM, CBM and  $E_{\text{F}}$  values were calculated from the UPS results, data for BCP/Ag were cited from literature; f) t-DOS characteristics for C60 control and Cl<sub>6</sub>SubPc/C60 ETLs based PSCs; g) Open circuit voltage ( $V_{\text{oc}}$ ) as function of illumination intensity for the C60 control and Cl<sub>6</sub>SubPc/C60 ETLs based PSCs.



**Figure 4**

a) Light stability tests of the control C60 devices (6 cells) and Cl<sub>6</sub>SubPc/C60 devices (6 cells) in inert atmosphere. The devices were un-encapsulated, and the I-V curves were recorded at certain time intervals; b) Thermal stability tests of the control C60 devices (6 cells) and Cl<sub>6</sub>SubPc/C60 devices (8 cells) at 80 °C under inert and dark environment; c) Damp heat stability tests of the encapsulated control C60 devices (5 cells) and Cl<sub>6</sub>SubPc/C60 devices (5 cells); d) Outdoor stability tests of the encapsulated control C60 devices (5 cells) and Cl<sub>6</sub>SubPc/C60 devices (9 cells) following the ISOS-O-1 protocol standard; e) Light stability of encapsulated Cl<sub>6</sub>SubPc/C60 cell in ambient under continuous 1 sun illumination and maximum power point tracking (MPPT).

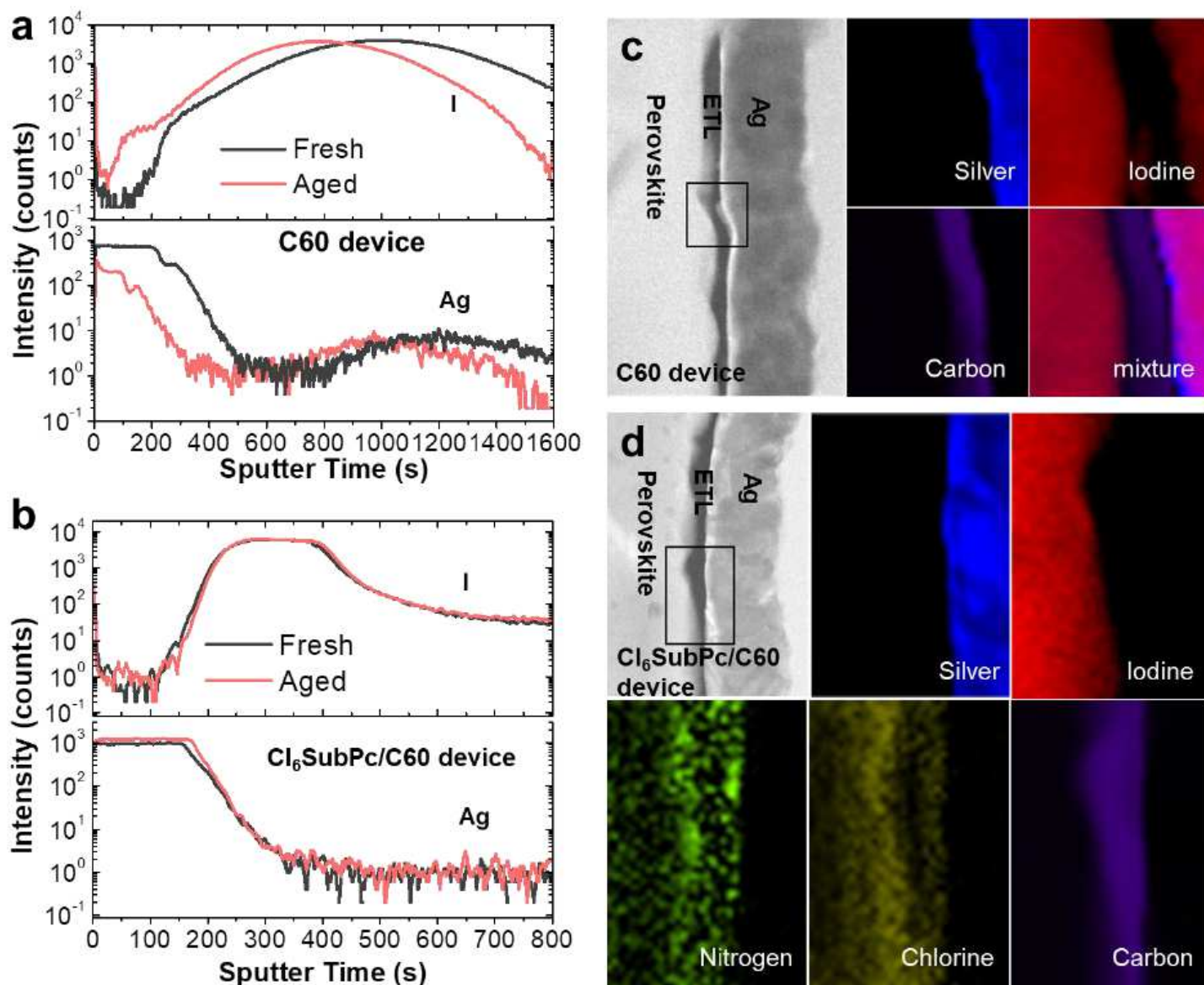


Figure 5

a) and b) Secondary-ion mass spectrometry (SIMS) profiles of I<sup>-</sup> and Ag<sup>+</sup> ions for the C60 control device (a) and Cl<sub>6</sub>SubPc/C60 device (b) before and after aging; c) and d) lateral EELS mapping of the aged C60 control device (c) and Cl<sub>6</sub>SubPc/C60 (d) device.

## Supplementary Files

This is a list of supplementary files associated with this preprint. Click to download.

- [Supportinginformation.pdf](#)